

# JOURNAL OF MECHANICS OF CONTINUA AND MATHEMATICAL SCIENCES

www.journalimcms.org



ISSN (Online): 2454-7190 Vol.-20, No.-10, October (2025) pp 118-137 ISSN (Print) 0973-8975

# DESIGN AND SIMULATION OF ROBUST DIGITAL VIDEO BROADCASTING CABLE (DVBC) USING QUADRATURE PHASE SHIFT KEYING (QPSK) MODEMS TECHNOLOGY WITHIN GAUSSIAN INTERFERING CHANNEL

Mohammed J. Alhasan<sup>1</sup>, Karar H. Hussein<sup>2</sup>

<sup>1</sup>Al-Najaf Technical Institute, Al-Furat Al-Awsat Technical University (ATU) Najaf, Iraq.

<sup>2</sup>Al-Kufa Technical Institute, Al-Furat Al-Awsat Technical University (ATU), Najaf, Iraq.

Email: mohammedj.alhasan@atu.edu.iq, kin.kra@atu.edu.iq https://doi.org/10.26782/jmcms.2025.10.00008

(Received: August 05, 2025; Revised: September 28, 2025; October 08, 2025)

#### **Abstract**

The main focus of this research is the design and simulation of a cable television DTTB SYSTEM THAT IS viewable in a OPSK demodulator, within a Gaussian noise interference channel. QPSK is the industry standard for encoding video signals. It's possible to find practical issues that prevent streaming. This, I would assume, is partially due to Equipment and encoding inconsistencies. For this research, QPSK has been used for encoding. This encoding will be made use as a part of the Gaussian channel for transmission and response. Adaptive equalization, but digital ones are being included to fix deficiency problems such as digital segregation and interference. Whenever data is comprehensively transmitted forth and back, the model forecasts that it would be possible to increase the transmission quality. In Particular, the model ensured a defined BER performance below 1 percent and provided reasonable throughput when SNR was in the range of 15 to 20 decibels. Broadly, the whole system can be divided into three functional blocks, which are the input and output sections (which are, in simpler terms, termed as communication channels) and the last block, which is the modulator block, and in this case, is the QPSK block. So, in a simple quest for this purpose, the system is designed in such a way as to limit the degradation of the received signal due to the presence of noise and interference in the Gaussian channel. Adaptation, or commonly known as equalization, is also the process of channel estimation, where the channel distortion is compensated for. It has improved in the simulation.

**Keywords:** Digital Video Broadcasting Communications, Quadrature Phase Shift Key (QPSK) Modulation, Gaussian Interference Channel, Digital Adaptive Equalizers, Throughput.

#### I. Introduction

The commencement of the principal phases of normalizing the digital TV broadcasting began in mid 90's expectation of digital multimedia broadcasting development over broadband communication. The venture named Digital Video Broadcasting (DVB) was begun by the European Telecommunication Standards Institute (ETSI) in the year of 1990. Its principal objective is to present a norm for digital multimedia services. The principal standard for satellite video broadcasting over GEO satellite was DVB-S, which utilizes the Forward Error Correction (FEC) strategy. Then ETSI presented a new standard called DVB-RCS (Return Channel Satellite). It gives the choice to utilize the same radio wire for the return connection at the collector by means of satellites. In the meantime, another venture, particularly called DVB-S2 for second-generation satellite broadcasting was presented by ETSI. It utilizes a new Forward Error Correction (FEC) method with a higher request tweak plot, dynamic choice of coding with channel state data [VII], [XXV], [II], [XIII], [XII]. The development of the satellite forward link incorporates displaying of the gateway transmitter, satellite, and client terminal collector with a channel pay strategy. Figure 1 shows the block graph for the satellite transmission chain in the forward link. The Bernoulli sequence generator is the absolute first block responsible for creating an irregular paired sequence. The result of this block is an outline that contains 1504 pieces. The yield from this Bernoulli generator is expected to make BBFRAME (Base Band Edge). The size will be equivalent to the information size of the BCH (Bose-Chaudhuri-Hocquenghem) encoder, which is connected with the coding rate. The use of forward error correction is to decrease the piece error rate in transmission. It is developed utilizing polynomials, which brings about cyclic error correcting codes. The result of the BCH encoder will be equivalent to the contribution of the LDPC encoder. It is viewed as a linear error control code. The coming about FEC outline is having a length of up to 64800 pieces. This block is trailed by a bit interleave. It makes lines in measurement design from the result of the LDPC encoder. The interleaved vector is handled by the regulation block. In this paper, OPSK and 32-APSK plans are utilized for tweaking. The raised cosine channel block is utilized to amplify the data rate transmission and to limit the transmission errors within the distributed data transfer capacity. It is then, at that point, trailed by a Digital to Analog Converter (DAC). Later DAC, the baseband signal is up-converted to transporter recurrence. Then the sign gets intensified at High Power Amplifier (HPA) [XIII], [XII], [XXIV]. At the satellite part, there will be linear distortion as well as non-linear distortion. The blemished size and group delay response of the OMUX and IMUX channels will present linear distortion as Inter-Symbol Interference (ISI). The equalization cycle will deal with the ISI. This is done by channel assessment in light of the information acquired from the channel. As star grouping warping and clustering, the non-linear distortion is presented by Voyaging Wave Tube Amplifier (TWTA) [XX], [XXVIII], [XIX], [XXIX]. At the recipient side, the result from the downlink module is given to the LNA. After that, the Added White Gaussian Noise (AWGN) block will add noise to the signal that is being sent from the modulator. It depends on the boundary arrangement. The noise variance estimate is determined by this block, and noise with zero mean is added to the flag. Then the signal is downconverted. Because of the nearby oscillator's flimsiness, the

sign gets distorted by the stage noise. Close to ADC, matched SRRCF is applied. To deal with linear distortion, the symbols are permitted to go through a linear adjuster. This should be possible after the timing and edge synchronization. Delicate demapper generates log-likelihood proportions. After the delinter leaving process, it is given as a contribution to the decoding stage. The delinter leaver block will get the result of the demodulator block as info. Then it performs an inverse interaction to make a sequential result for the LDPC decoder. It is then trailed by the BCH decoder. Besides, the Channel Compensation Strategy will operate against the Pre-distortion that compensates for the impact of ghastly regrowth. Data pre-distortion will protect the signal range and be applied to the star grouping symbol preceding heartbeat formation. Static data pre-distortion represents static non-linearity in the channel. The pre-distorted star grouping focuses are stored in the lookup table. Dynamic data pre-distortion repays memory impacts in the channel. Figure 1 shows a general block diagram of a digital video broadcasting modem [XX], [XXVIII], [XIX], [XXIX], [XV], [IX].

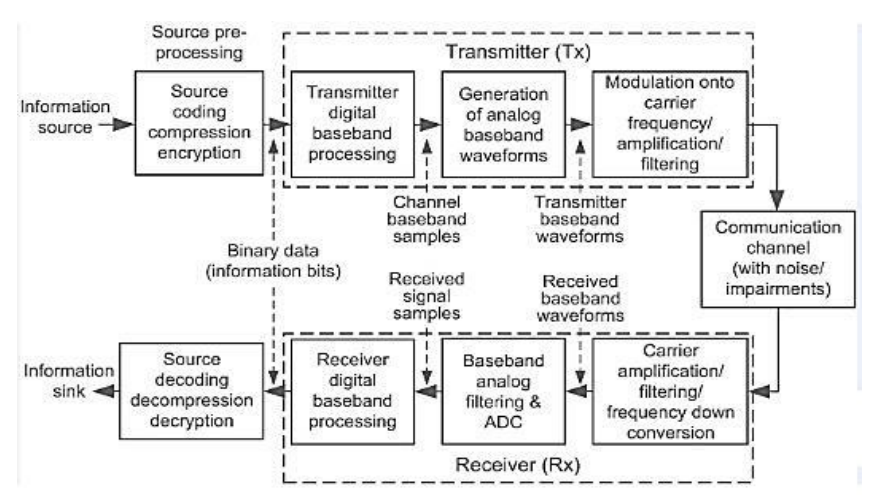


**Fig. 1.** General block diagram of digital video broadcasting modem [XX], [XXVIII], [XIX], [XXIX], [XV], [IX].

In fact, Digital Video Broadcasting (DVB) might be regarded as a set of standards for digital transmission of video and audio streams, as well as data transmission. It distributes data through a variety of methods such as satellite, cable, terrestrial television, handheld terrestrial television, or Microwave. Figure 1 illustrates the SC-FDMA construction diagram. Suppose the unique base station against uplink client U is provided. On the transmitter end, which relied on modulation schemes, the encoded data is transformed towards a multi-stage evolution of sophisticated codes. The formed complicated symbols are then split into blocks, each with M complicated symbols, along with the employed DFT. After DFT, the wave could be expressed as [VI], [VIII], [XXIII], [XIV], [XXII]:

$$X(k) = \sum_{m=0}^{M-1} x(n)e^{-\frac{j2\pi nk}{M}}$$
 (1)

Such that: M denotes the entered block size,  $\{x(n) : n=0,1,2,...,M-1\}$  indicates the transmitted complex info symbols in which the result of FFT is mapped to N (N>M) orthogonal subcarriers, followed by N-point IFFT to alter to the time-domain complex signal. The ultimate clients' sum that could be sent together could be expressed as below [12-18]:

$$Q = \frac{N}{M} \tag{2}$$

Whereas, Q: denotes the ultimate client's sum, in which the system could be covered. M: denotes the input block size with the sum of subcarriers allocated for every client. Also, N represents the overall subcarrier with the IFFT size. Note that other clients might utilize (N-M) subcarriers. Hence, multiple access is obtained, or at times, the resting subcarriers are zero-padded. Moreover, the achieved waveform after the IFFT might be represented as below [VI], [VIII-XXIII], [XXII], [XXII];

$$\bar{x}(n) = \frac{1}{N} \sum_{l=0}^{N-1} x(l) e^{-\frac{j2\pi nl}{N}}$$
 (3)

Such that,  $\{x(l): l = 0,1,2,..., N-1\}$  denotes the frequency band sequences before the subcarriers mapping process.  $\bar{x}(n)$ , represents samples in the time domain behind the IFFT operation.

#### Peak to Average Power Ratio (PAPR)

Actually, PAPR might be determined as the ratio of peak to average power. It is a basic factor in uplink communication and is commonly estimated for the transmitted waveform. Signal-to-peak ratio is one of the crucial issues which have devoted authors due to its crash on the error rate of the info. A larger value of the peak-to-average ratio tends to a lower transmitter capacity, which results in a higher rate of data errors. The succeeding expression might describe the hypothetical relationship between PAPR (in dB) and power efficiency of the transmission [VI], [VIII], [XXIII], [XXII], [XIV], [XXII], [XIV], [XII].

$$\eta = \eta_{max} \cdot 10^{-\frac{PAPR}{20}} \tag{4}$$

Whereas  $\eta$  denotes the power performance and  $\eta_{max}$  to the ultimate power performance. Through the previous equation, it's obvious that when the PAPR advances, the transmission power performance is minimized. The peak-to-average ratio might be evaluated for the communicated waveform x(t) along the incoming expression:

$$PAPR = \frac{peak\ power\ of\ x(t)}{average\ power\ of\ x(t)} = \frac{Max_{0 \le t \le NT}|x(t)|^2}{(\frac{1}{NT})\int_0^{NT}|x(t)|^2dt} \tag{5}$$

The PAPR beyond pulse shaping, symbol rate sampling would provide the exact PAPR as the continuous, thus, we represent the PAPR without pulse shaping with symbol rate sampling as follows:

$$PAPR = \frac{\max_{n=0,1,\dots N-1} |x(n)|^2}{\frac{1}{N} \sum_{0}^{N-1} |x(n)|^2}$$
 (6)

The PAPR is usually expressed statistically by the Complementary Cumulative Distribution Function (CCDF) of PAPR, that is, the probability that PAPR is higher than a certain PAPR amount PAPRO ( P<sub>r</sub>{PAPR>PAPRO}). The entire system efficiency, as well as the rigor with cost of transmitter installation, is affected by the high PAPR rate. The waveforms are transmitted to the base station through the uplink by being transmitted along all regional devices. This will communicate with the access approach, which ensures that the transmitting power of the device is massive sufficient to transmit a waveform to the base station. The system needs a wide power amplifier with a large linear space if the PAPR amount is huge. Miniature PAPR has been found to result in enhanced energy efficiency, which promotes longer battery life. Figure 2 displays the PAPR performance for various modulation schemes.

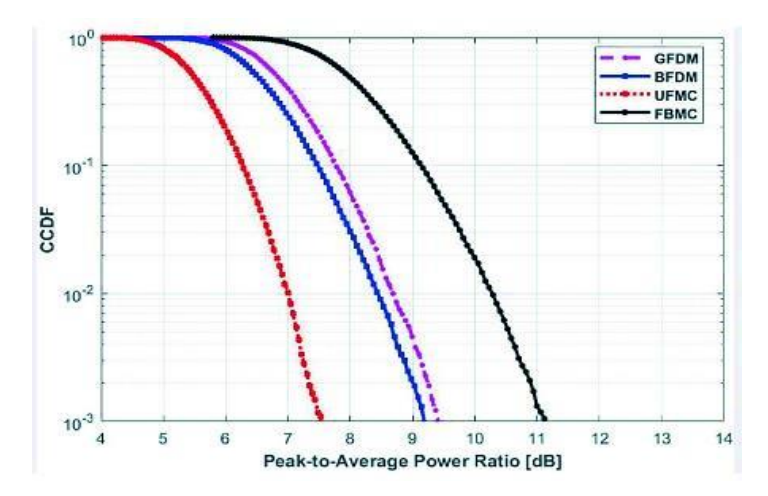


**Fig. 2.** The PAPR performance for various modulation schemes [VI], [VIII], [XXIII], [XXII], [XVI], [XVI], [XI].

#### **Equalizers Techniques**

Equalizer models are part of modern methods that could be utilized to evaluate interference problems in data transmitted over various communication channels. Different types of equalizers work to predict the shape of the transmission channel and produce a response opposite to the effect of the spectral response of the transmission channel to eliminate inter-symbol interference (ISI) among the symbols transmitted through it. The efficiency of equalizer operations depends on the strength of the boost and the ability of these systems to eliminate the effects of the transmission channel. These equations are divided into regular and smart equations that use artificial intelligence methods [VIII], [XXIII], [XXII], [XIV], [XXI], [XVI], [XII], [XIII], [XXIII], [XXI

$$y(n) = w^{T}(n-1)u(n) \tag{7}$$

$$e(n) = d(n) - y(n) \tag{8}$$

$$w(n) = w(n-1) + \mu e(n)u^*(n)$$
(9)

$$\xi = E[e^2(n)] - E[d^2(n)] - 2w^T P + w^T R w$$
 (10)

Besides LMS/NLMS, we evaluate a linear MMSE equalizer and a decision-feedback equalizer (DFE) with Lf forward and  $L_b$  feedback taps. MMSE minimizes the mean-square error in closed form; DFE cancels post-cursor ISI via detected symbols. Unless otherwise stated, we use  $L_f = 7$ , Lb = 6, LMS/NLMS step size  $\mu$ =3×10<sup>-3,</sup> and RLS forgetting factor 0.99. All equalizers are trained on the same pilot length and tested on the same multipath channel and SNR as defined in Sec. III.

**Table -1.** Per-symbol complexity (multiplications).  $L_f/L_b$ : forward/feedback taps; MMSE via RLS.

Equalizer	Per-symbol complexity (multiplies)			
LMS	≈2L <sub>f</sub>			
NLMS	≈3L <sub>f</sub>			
MMSE (RLS)	$\mathrm{O}(L_f^3)$ update; pre-solve $((L_f^{23})$			
DFE	$pprox 2L_f + 2L_b$			

Whereas, y(n) represents the adaptive filter yield, e(n) indicates the estimated error between filter yield and needed signal d(n) at n step, d(n), denotes the planning progression through critical recognized parameters (likewise called a pilot signal), is expected to prepare those adaptive coefficients. w(n). Adequate readiness game plan for realized variables ought to be an opportunity to be available for convergence assurance. Condition (9) would be such weights w(n) overhaul operation for the LMS algorithm, whereas  $\mu$  denotes the variation factor, adjusted through the radio antenna wire handling gain displayed as depicted in the numerical explanation below:

$$P_G = 10Log_{10}(\frac{B}{R_b}) \tag{11}$$

$$0 \le \mu \le \frac{1}{\lambda_{max}} \tag{12}$$

Where B addresses the channel bandwidth of the CDMA technology, having an information bit rate Rb in bits/sec. Besides, the image (\*) implies the mind-boggling form of the input signal u(n). The convergence states constrained as for venture measure  $\mu$  might be provided as introduced in Eq.(12). Such that,  $\lambda$ max indicates the autocorrelation array R greatest eigenvalue, and when  $\mu$  is taken to turn out to be close to nothing, hence the convergence will be gradual. Then again, in the event that

 $\mu$  remains large, consequently convergence will be extremely quick, yet the stability will be an issue. Consequently, it is likely to pick  $\mu$  amidst restricted imperatives as displayed in relation (12). In addition,  $\xi$  is the presentation function that presents the filter tap-weight vector W, quadratic action in terms of MSE. Finally, R denotes the autocorrelation framework of filter inputs that is composed such that:

$$R = E[u(n)u^{T}(n)] \tag{13}$$

Further, P denotes the cross-correlation array between inputs against the wanted signal and might be expressed as:

$$P = E[u(n)d(n)] \tag{14}$$

Next, by solving relation (10) against optimal results, one could achieve:

$$w_0 = PR^{-1} (15)$$

The above condition is known as the Wiener-Hopf equation. On the off chance that P and R are not open, we ought to comprehend Wiener-Hopf directly. Then, we use an iterative look method beforehand, which starts with a basic estimate for  $w_0$ , say w(0), and a recursive sweep technique that needs a great deal of cycles on meet ought to  $w_0$  is employed. For a starting estimation to  $w_0$  through n=0, that tap-weight vector into the n<sup>th</sup> cycles might be introduced as W(n), which finally depends on  $\mu$  for convergence to come by ideal outcome  $w_0$  to cutting-edge savvy radio antenna. Thus, by exhibiting the inclusion for number through components of  $(N_e)$  that finally head, to obtain the best MSE [VI], [VIII], [XXIII], [XXII], [XIV], [XXI], [XII].

Then again, the NLMS algorithm uses information subject to the step size  $\mu$  for each cycle, done likewise to beat the requirement of assessing the eigen sum for the autocorrelation lattice R, or its successor for the ideal suitable step size nomination. If for such an algorithm, the weights refreshing piece of condition (9) will be adjusted while any remaining pieces of the function supporting comparable in like manner as that for the LMS conditions [VIII], [XXIII], [XXII], [XIV], [XXI], [XVI], [XI], [XXVI]. So, the weight refreshing condition for the NLMS computation might be commonplace as:

$$w(n) = w(n-1) + \mu e(n) \frac{u^*(n)}{\varepsilon + u^H(n)u(n)}$$
 (16)

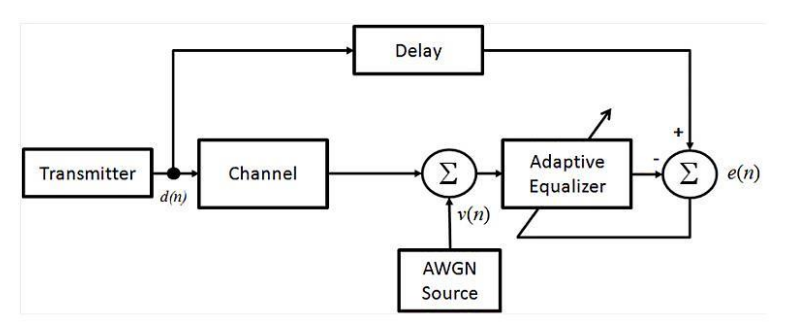


Fig. 3. Demonstration of general equalizer system structure [16-23].

#### II. Related Studies

In 2017, Malkowsky, S., et. al., [IX], focused on the design of a structure for a huge MIMO test-bed by considering several fundamental demands like the frame format, waveform signal scheme, as well as the complexity of the system. The plan was approved inside the Lund College gigantic MIMO equipment. The proposed plan upholds up to 100 radio wires and in excess of 50 FPGAs. In a time-division duplex (TDD) (LTE-like TDD) power, an OFDM modulation makes it possible to accommodate up to 12 clients at the exact frequency or instant. The tests were carried out both inside and outside. In 2018, Hasan, W.B., et. Al., [III] have proposed a second hardware test-bed with a base station that has a spectral efficiency of 145.6 bis/s/Hz, which might serve 22 clients. In front of the base stations, a 128-element receiving patch antenna array using a distance of 24.8 m from the transmitter was set up. The time-division duplex (TDD) enormous MIMO framework works at a transporter recurrence of 3.51 GHz with a 256-quadrature adequacy adjustment (QAM) plot. A zero forcing (ZF) or Minimum Mean Square Error (MMSE) was employed to guarantee a robust info transmission, with estimation of the channel carried out cyclically every 5 milliseconds. In 2018, Batra, A., et. al. [IV] created a mm-wave MIMO test-bed at the Institute of Digital Signal Processing (DSV) at the University of Duisburg-Essen, to initially operate at frequencies below 6 GHz. Over the FPGA, DSP, and GPU, it was employed in a heterogeneous environment. The stage could be reached somewhat through VPN by scholastic and modern scientists. In 2018, Batra, A., et. al., [VI], Accelerate the channel estimation based on the Least Squares (LS) algorithm with the uplink OFDM unique-client MIMO model demodulation using a GPU. The application was carried out in an ORBIT test-bed, such that various configurations of the system's response were evaluated in relation to the number with the length of the Fast Fourier Transform (FFT). The researchers achieve that by increasing the number of antennas and the length of the FFT reduces GPU performance. As a result, they suggested parallelizing the application, employing allocated algorithms, with employing an allocated server in subsequent work. In 2018, Chang, Y.-K., et. al. [VIII] suggest a summed up FDM (GFDM) beneficiary plan in view of index modulation (IM) [17], taking into account a blurring direct factor in time. Self-created inter-carrier interference (ICI) and intersymbol interference (ISI) are both eliminated by the designed architecture. Such issues were brought about by the shaping filters employed using GFDM. It utilizes two-phase rotations for multipath communication in environments with rapid fading. The ideal

stage turns are obtained by expanding the carrier-to-interference ratio (CIR). In 2019, Gokalgandhi, B., et. al., [XXIII], discussed the accelerating channel estimation and demodulation of uplink OFDM symbols for huge scale antenna models utilizing GPU. In 2019, Kamran Shereen, M., et. al., [XXII] conducted a comprehensive review of reconfigurable antennas in general for use in 5G applications. They looked at and discussed a number of the prototypes that were suggested for MIMO and cognitive radio models. In 2019, Sharief, A.H., et. al., [XIV], have proposed a brandnew frequency-discrete wavelet-based MIMO-OFDM framework known as MIMO-RDWT-OFDM. The spectral efficiency of the transceiver is greatly improved by employing the newly developed frequency-discrete wavelet transform, which does not include a down-sampling step in the decomposition tree. Additionally, since it is more resistant to noise, it could be used in AWGN channels like the Rayleigh fading model. In 2022, Luther, E., [XXI], suggested one of the first completely approved and practical monstrous MIMO test beds with regard to a coordinated effort between the College of Bristol and Lund College, essential to Public Instruments (NI). The MIMO-OFDM model is intended for spectral efficiency analysis. It has a bandwidth of 20 MHz, a sampling rate of 30.72 MS/s, and it might be utilized in the frequency range of 1.2-6 GHz. Additionally, it can accommodate up to ten users per time or frequency slot and 128 antennas. A time slot lasts 0.5 milliseconds, utilizes 1200 subcarriers, and has a spectral efficiency of 145.6 bits/s/Hz.

#### II. Methodology

In this section, the mechanism for designing and implementing the proposed study model is reviewed. Figure 4 shows a MATLAB simulation diagram for a digital video transmission system using QPSK embedding.

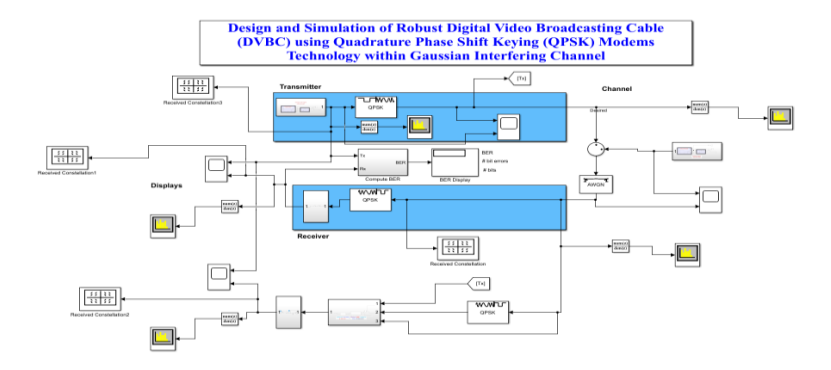


**Fig. 4.** Matlab simulation diagram for a digital video transmission system using QPSK embedding.

We note from Figure 4 the details of the software simulation of the model proposed in this study. The system consists of three basic parts: the transmitting section, the communications channel section, and the receiving section. A modulation technique of QPSK has been employed to upload data with a Gaussian channel representation, in addition to applying a digital adaptive equalizer system. Also, the utilized dataset has been provided from a random signal generator utility supported by MATLAB

software. Figure 5 displays the random signal generator utility used for dataset support.

#### Analogue Video Signal Generator unit

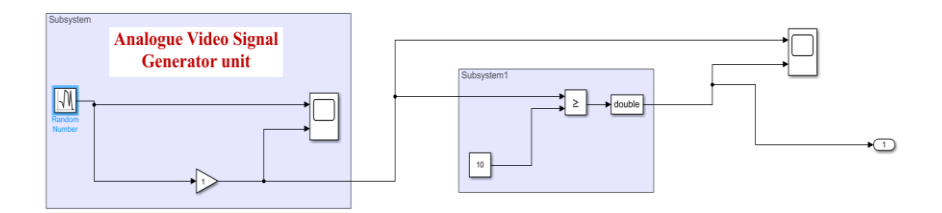


Fig. 5. The random signal generator utility is utilized for dataset support.

Also, the structure of the proposed video broadcasting model using the QPSK Gaussian channel technique is demonstrated in Figure 6.



**Fig 6.** Demonstration flow chart of the proposed video broadcasting model using the QPSK Gaussian channel technique.

By looking at Figure 6 above, the signal flow diagram of the model proposed in the study begins with identifying and creating the data set for video signals, configuring it, and arranging it through the data processing unit. These data are used as sources of transmitted information, followed by applying the QPSK transmission system and then the Gaussian channel. The adaptive equalizer is then used to eliminate extraneous signal interference problems by estimating the characteristics of the communication channel. This is followed by verifying the amount of productivity and receiving efficiency, while displaying the results and metrics. Moreover, the design settings and parameters employed in the proposed model are listed in Table 2.

**Table 2:** The design settings and parameters employed in the proposed model.

System Type	Sampling Frequency (f <sub>s</sub> )	Operating Frequency (BW)	Design Setting Details	Design Type	Notes
Video Data Generator	1 GHz	(10-50) MHz	Mean=10 Variance=0. 1 Seed=3	Random Signal Generato r	Employ ADC Rb=10 M bps
Transmitter System	10 GHz	1 GHz	Bit Rate (Rb)=2 M bps	QPSK	Binary Format with 90 <sup>0</sup>
Communica tion Channel	10 GHz	(0.1-10) GHz	SNR= 5 dB	AWGN With the Interferen ce Channel	Number of bits per symbol=1
Receiver System	10 GHz	1 GHz	Integration period (number of samples): 8	QPSK	Binary Format with 90 <sup>0</sup>

# III. Results & Discussion

The results of implementing the proposed video broadcasting model have been achieved using MATLAB software application. This study used simulation-based experiments as a working methodology with premium MATLAB tools and libraries to conduct training and testing using the loaded dataset. The effectiveness of the proposed technique was evaluated through adopted metrics, including spectral efficiency, power efficiency, and bit error rate. The proposed model was trained and tested using data generated from the simulation environment, and the resulting results and diagrams were extracted.

Figure 7 reports BER vs.  $E_b/N_0E$  for QPSK, 16-QAM, and 32-QAM with 95% confidence bands. Table 3 summarizes spectral efficiency and the required  $E_b/N_0E$  at BER =10<sup>-3</sup>.

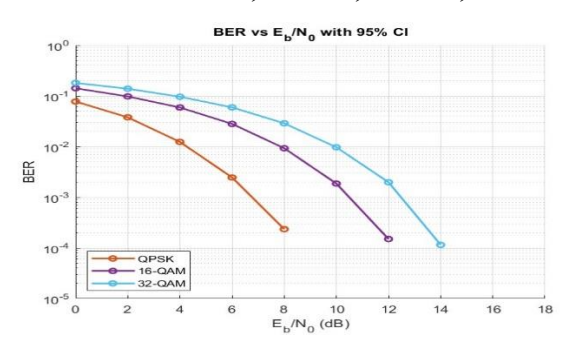


**Fig. 7.** BER vs. E<sub>b</sub>/N<sub>0</sub> for QPSK, 16-QAM, and 32-QAM over AWGN; shaded bands indicate 95% confidence intervals.

QPSK shows the highest robustness at low SNR. Higher-order constellations increase spectral efficiency but require additional SNR for the same BER ( $\approx +3.8$  dB for 16-QAM and  $\approx +5.9$  dB for 32-QAM vs. QPSK at BER = $10^{-3}$ .

**Table 3 :** Spectral efficiency and required  $E_b/N_0$  at BER =  $10^{-3}$  (AWGN)

Mod	M	SpectEff (bits/s/Hz)	$Eb/N0 @ BER = 10^{-3} (dB)$
QPSK	4	2	6.83
16-QAM	16	4	10.62
32-QAM	2-QAM 32 5		12.69

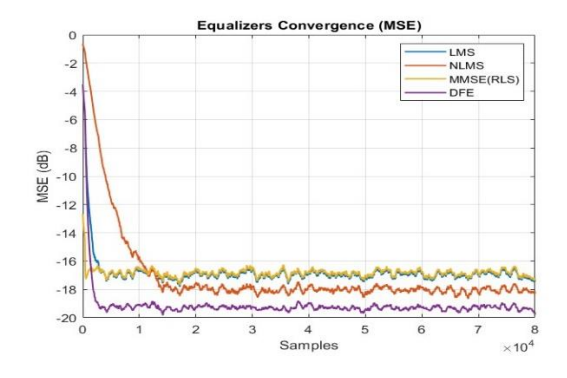


**Fig. 8.** Equalizer learning curves (MSE vs. samples) under the same multipath channel and SNR. DFE attains the lowest steady-state MSE; MMSE (RLS) converges rapidly; NLMS/LMS are lighter but settle higher.

DFE reduces post-cursor ISI via feedback, yielding the best residual error. MMSE (RLS) minimizes MSE in closed form and converges fast; NLMS stabilizes slightly faster than LMS due to input-power normalization, but both exhibit higher steady-state MSE compared with DFE.

Figure 8 shows the results of information data extraction in the time domain, polar domain, and spectral domain.

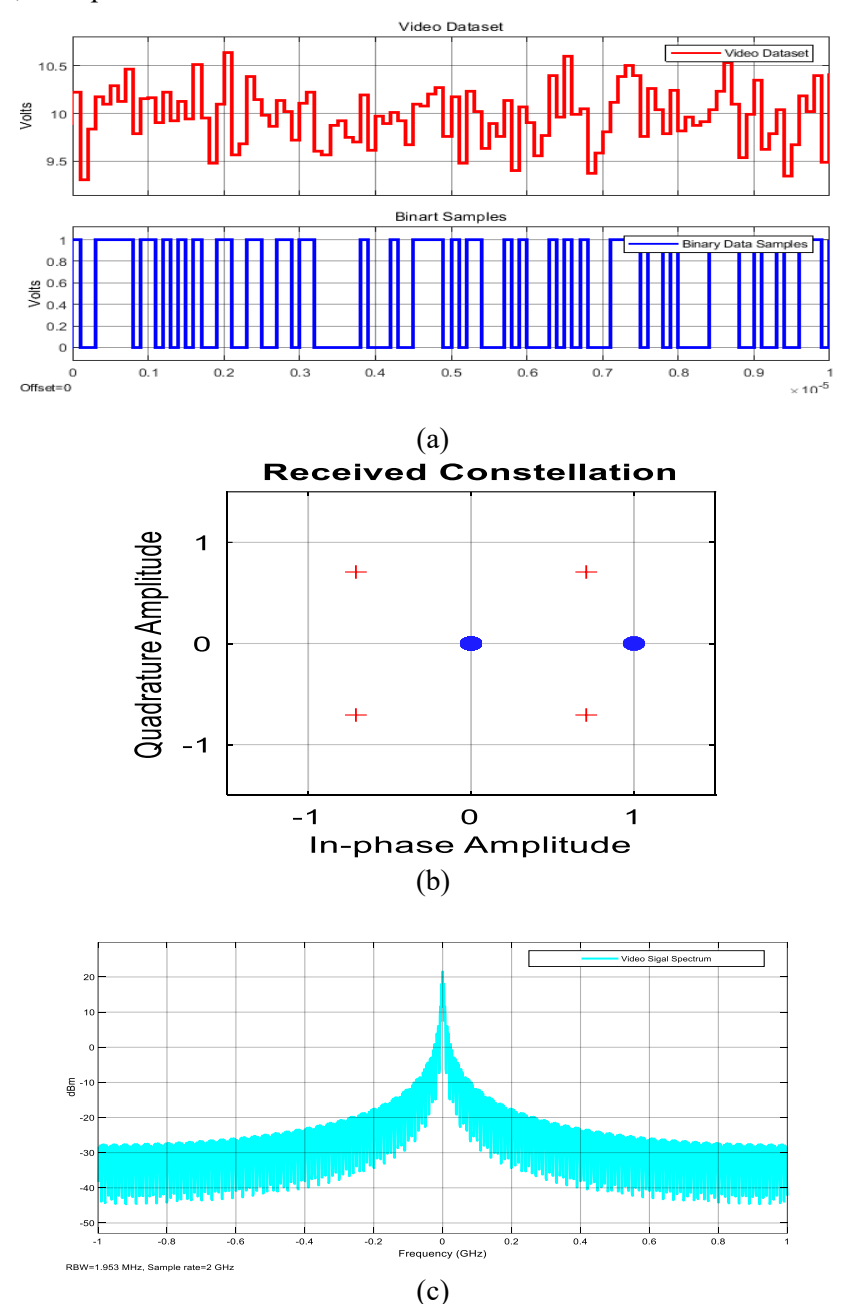


**Fig. 9.** The simulated results of the video transmitted dataset, (a) Time domain, (b) Polar plot, and (c) Frequency domain.

One could recognize from Figure 9 that the generated data ranges in video wave frequencies up to 100 MHz with a polar bias of zero degrees in preparation for sending it over the communications channel using QPSK modulation. Next, the

transmission results of the proposed QPSK modulation scheme have been presented in Figure 8 after passing through the AWGN channel with time, polar, and spectral views.

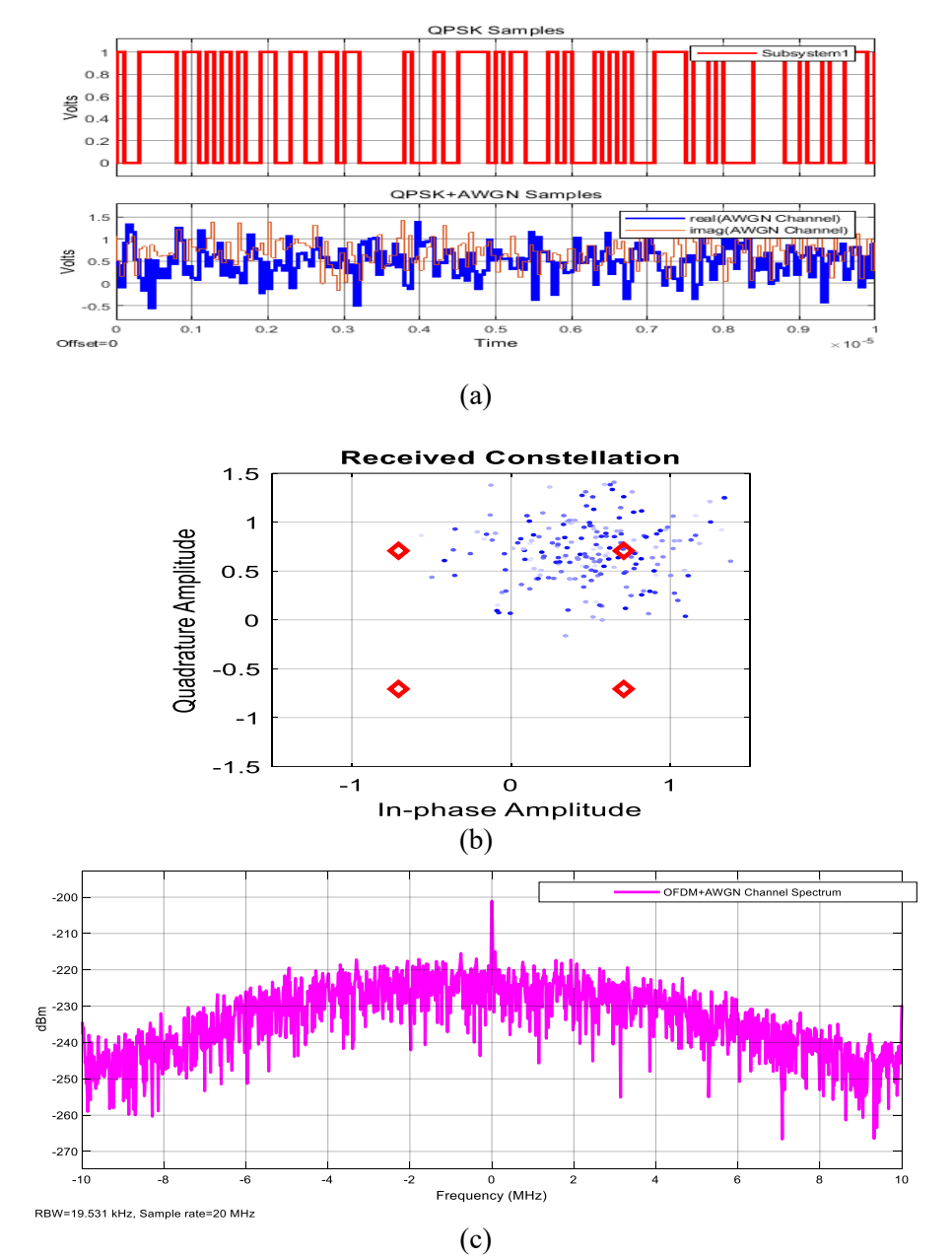


**Fig. 10.** The simulated results of the QPSK/AWGN transmitted signal, (a) Time domain, (b) Polar plot, and (c) Frequency domain.

By looking at the details of Figure 10, one notices that the data modulation results show a polar bias of 45 degrees according to the digital modulation design, in addition to the distribution of the energy of the transmitted data on high carrier

frequencies in the spectral domain. Also, it is possible to observe the dispersion of signals in polar polarization due to the effects of noise signals in the Gaussian communication channel. This is followed by a review of the results of the effect of the QPSK demodulator system on the received signal, as shown in Figure 9 in the time, polarity, and frequency fields.

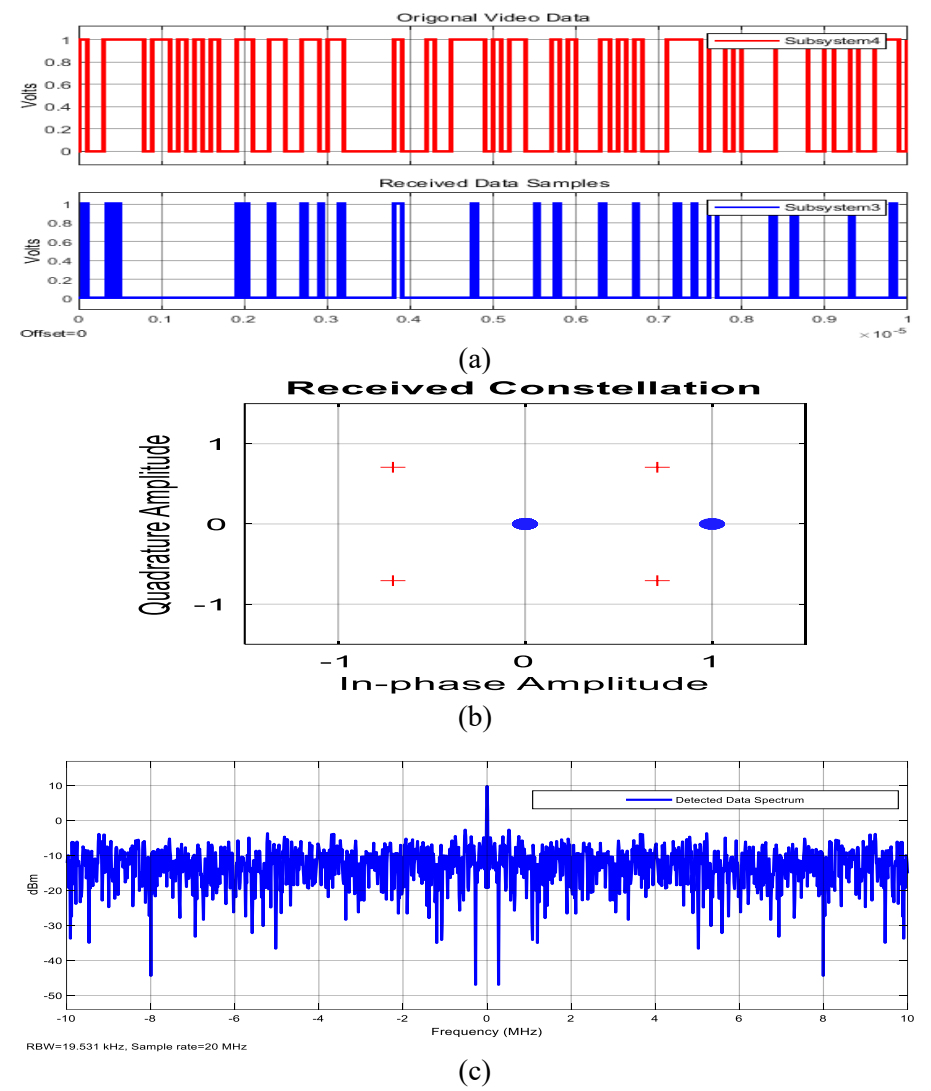


**Fig. 11.** The simulated results of the QPSK demodulator received signal, (a) Time domain, (b) Polar plot, and (c) Frequency domain.

By looking at Figure 11, one could observe the success of the QPSK demodulation system in extracting information from the transmitted waves, but with some errors due to the noise effects of the Gaussian communication channel. We might also observe the effect of the Gaussian transmission channel on the transmitted data set, such that the data values are different while maintaining the phase modulation, as shown in Figure 11(b). We also notice the effect of noise and interference in the

received data spectra, as shown in Figure 11(c). Moreover, the results of the effect of the adaptive equalizer system on the received signal have achieved as shown in Figure 11 in the time, polarity, and frequency domains. The idea of this paper can be developed further by techniques reported in [XXVI-XXXIV].

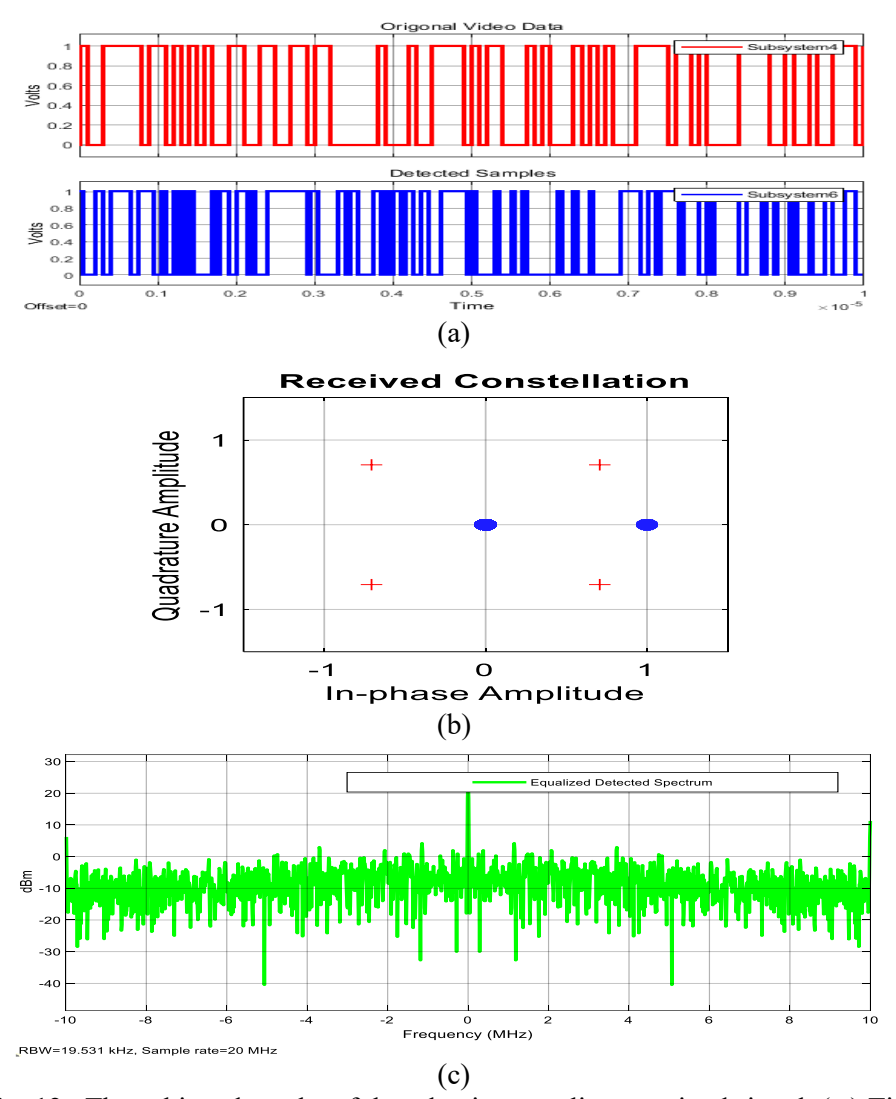


**Fig. 12.** The achieved results of the adaptive equalizer received signal, (a) Time domain, (b) Polar plot, and (c) Frequency domain.

Looking at Figure 11, it is possible to observe the success of the adaptive equalizer system in extracting information from the transmitted waves, with low error rates due to the performance of the adaptive equalizer system in canceling the effects of noise and estimating the response of the Gaussian communication channel. Also, the effect of the adaptive equalizer technology on the phase response is shown in Figure 12(b), where it appears identical to the transmitter response. Moreover, the results of the effect of the adaptive equalizer system on the received signal spectra have been

achieved as shown in Figure 12(c) in the frequency domains. Furthermore, the bit error rates (BERs) or throughput results with and without an adaptive equalizer have been evaluated for the digital video signal broadcasting using QPSK Gaussian channel communication, as displayed in Figure 13.

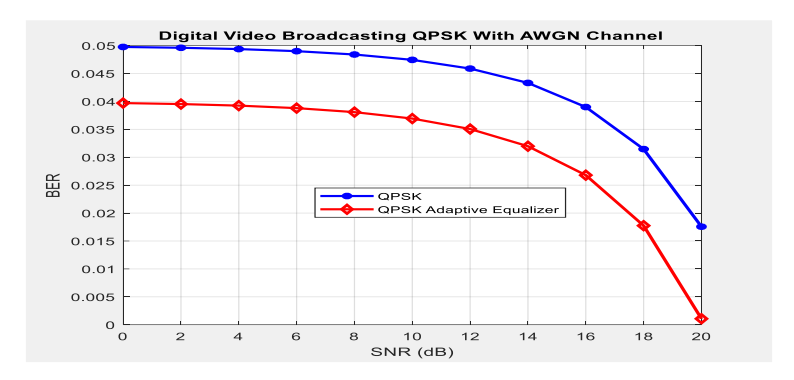


**Fig. 13.** The bit error rates BER with/without the adaptive equalizer technique for the digital video signal broadcasting using QPSK Gaussian channel communication.

By looking at the results shown in Figure 13 above, one could notice the improvement in the response of the error rate chart after adding the adaptive equalizer technology to the system, which shows an improvement of more than 20% at SNR 2 dB and reaches 50 at SNR 20 dB, which shows improved reception. Finally, Table 4.

System Type	SNR (dB)	BER	Error Rate Enhancement	Efficiency	Detected Data Quality
Without an Adaptive equalizer	10	0.05 -15	20-30%	Bad	High Distortion
	20	2*10 <sup>-2</sup> -20	25-35%	Medium	Medium Distortion
With an Adaptive equalizer	1	10 <sup>-3</sup> -30	50%	Very Good	Low Distortion

**Table 4**: Comparison of the obtained results.

#### IV. Conclusions

This research discussed that digital video communications suffer from a range of compatibility issues, such as incompatibility of the streaming platform or equipment with the transmitter or software being used, as well as encryption issues, which can be caused by the failure of streaming software to properly encode video and audio data. The design and simulation of a digital video communications system was reviewed using the technique of embedding a quadrature phase shift key within the Gaussian interference channel. Transmission and reception were also evaluated, and an adaptive digital equalizer will be proposed to address digital dispersion and interference problems. An error rate of less than 0.1% and improved receive throughput of -30 dB were achieved at a signal-to-noise ratio (SNR) of 20 dB.

#### **Conflict of Interest:**

There was no relevant conflict of interest regarding this paper.

#### References

- I. Ahn, C., et al. "Implementation of an SDR Platform Using GPU and Its Application to a 2×2 MIMO WiMAX System." *Analog Integrated Circuits and Signal Processing*, vol. 69, no. 1, 2011, pp. 107–120. 10.1007/s10470-011-9645-7.
- II. Arrano, Hernan F., and Cesar A. Azurdia-Meza. "OFDM: Today and in the Future of Next Generation Wireless Communications." 2016 IEEE Central America and Panama Student Conference (CONESCAPAN), 2016, pp. 1–6. 10.1109/CONESCAPAN.2016.7815720.
- III. Batra, A., et al. "A Massive MIMO Signal Processing Architecture for GHz to THz Frequencies." *Proceedings of the 2018 First International Workshop on Mobile Terahertz Systems (IWMTS)*, IEEE, 2–4 July 2018, pp. 1–6. 10.1109/IWMTS.2018.8439066.
- IV. Batra, A., et al. "A Massive MIMO Signal Processing Architecture for GHz to THz Frequencies." *Proceedings of the 2018 First International Workshop on Mobile Terahertz Systems (IWMTS)*, IEEE, 2–4 July 2018, pp. 1–6. 10.1109/IWMTS.2018.8439066.
- V. Caire, Giuseppe, et al. "Bit-Interleaved Coded Modulation." *IEEE Transactions on Information Theory*, vol. 44, no. 3, 1998, pp. 927–946. 10.1109/18.669123.
- VI. Chang, Yu-Kuo, and Fu-Berg Ueng. "A Novel Turbo GFDM-IM Receiver for MIMO Communications." *AEU International Journal of Electronics and Communications*, vol. 87, 2018, pp. 22–32. 10.1016/j.aeue.2018.02.011.
- VII. Foo, S. "Liquid-Crystal Reconfigurable Metasurface Reflectors." *IEEE International Symposium on Antennas and Propagation & USNC/URSI National Radio Science Meeting*, July 2017, pp. 2069–2070. 10.1109/APUSNCURSINRSM.2017.8072855.
- VIII. Gardner, W. A. "Exploitation of Spectral Redundancy in Cyclostationary Signals." *IEEE Signal Processing Magazine*. 10.1109/79.366549.
  - IX. Gokalgandhi, Bhushan, et al. "Accelerating Channel Estimation and Demodulation of Uplink OFDM Symbols for Large Scale Antenna Systems Using GPU." 2019 International Conference on Computing, Networking and Communications (ICNC), IEEE, 18–21 Feb. 2019, pp. 955–959. 10.1109/ICCNC.2019.8685564.
  - X. Hasan, W. B., et al. "Real-Time Maximum Spectral Efficiency for Massive MIMO and Its Limits." *IEEE Access*, vol. 6, 2018, pp. 46122–46133. 10.1109/ACCESS.2018.2865946.

- XI. Hoda, B., and B. Babamir. "Enhancing Efficiency of Software Fault Tolerance Techniques in Satellite Motion System." *Journal of Information Systems and Telecommunication (JIST)*, vol. 5, no. 20, 2017, pp. 236–241. URL: https://www.jist.ir/article 22595.html.
- XII. Ijiga, O. E., et al. "Review of Channel Estimation for Candidate Waveforms of Next Generation Networks." *Electronics*, vol. 8, no. 8, 2019, p. 956. 10.3390/electronics8080956.
- XIII. Jangir, D., et al. "Performance Analysis of LTE System for 2×2 Rayleigh and Rician Fading Channel." 2020 International Conference on Smart Electronics and Communication (ICOSEC), 2020, pp. 961–966. 10.1109/ICOSEC49089.2020.9215423.
- XIV. Shereen, M. Kamran, et al. "A Brief Review of Frequency, Radiation Pattern, Polarization, and Compound Reconfigurable Antennas for 5G Applications." *Journal of Computational Electronics*, vol. 18, 2019, pp. 1065–1102. 10.1007/s10825-019-01369-y.
- XV. Liu, Fan, et al. "Joint Radar and Communication Design: Applications, State-of-the-Art, and the Road Ahead." *IEEE Transactions on Communications*, 2020. 10.1109/TCOMM.2020.2973976.
- XVI. Luther, Erik. 5G Massive MIMO Testbed: From Theory to Reality. National Instruments, 2014. URL: https://www.ni.com/en-rs/innovations/white-papers/14/5g-massive-mimo-testbed--from-heory-to-reality--.html.
- XVII. Malkowsky, Steffen, et al. "The World's First Real-Time Testbed for Massive MIMO: Design, Implementation, and Validation." *IEEE Access*, vol. 5, 2017, pp. 9073–9088. 10.1109/ACCESS.2017.2707539.
- XVIII. Mokhtari, Zahra, et al. "A Survey on Massive MIMO Systems in Presence of Channel and Hardware Impairments." *Sensors*, vol. 19, no. 1, 2019, p. 164. 10.3390/s19010164.
- XIX. Paul, B. S., and R. Bhattacharjee. "MIMO Channel Modeling: A Review." *IETE Technical Review*, vol. 25, no. 6, 2008, pp. 315–319. 10.4103/0256-4602.46478.
- XX. Qiao, Guangjian, et al. "Channel Estimation and Equalization of Underwater Acoustic MIMO-OFDM Systems: A Review." *Canadian Journal of Electrical and Computer Engineering*, vol. 42, no. 4, 2019, pp. 199–208. 10.1109/CJECE.2019.2931177.
- XXI. Roger, S., et al. "Fully Parallel GPU Implementation of a Fixed-Complexity Soft-Output MIMO Detector." *IEEE Transactions on Vehicular Technology*, vol. 61, no. 8, 2012, pp. 3796–3800. 10.1109/TVT.2012.2203925.
- XXII. Saad, Walid, et al. "A Vision of 6G Wireless Systems: Applications, Trends, Technologies, and Open Research Problems." *IEEE Network*, vol. 34, no. 3, 2020, pp. 134–142. 10.1109/MNET.001.1900287.
- XXIII. Sethi, Abhishek, et al. "Mobility and QoS Based Cross Network for ICN Vehicular Communication." *Procedia Computer Science*, vol. 171, 2020, pp. 897–906. 10.1016/j.procs.2020.04.097.

- XXIV. Sharief, A. H., and M. S. Sairam. "Performance Analysis of MIMO-RDWT-OFDM System with Optimal Genetic Algorithm." *AEU International Journal of Electronics and Communications*, vol. 111, 2019, 152912. 10.1016/j.aeue.2019.152912.
- XXV. Singh, H., et al. "Performance Analysis and BER Comparison of OFDM System for 4×4 MIMO Fading Channel in Different Modulation Scheme." 2020 Third International Conference on Smart Systems and Inventive Technology (ICSSIT), 2020, pp. 255–259. 10.1109/ICSSIT48917.2020.9214109.
- XXVI. Wen, Feng, et al. "A Survey on 5G Massive MIMO Localization." *Digital Signal Processing*, vol. 94, 2019, pp. 21–28. 10.1016/j.dsp.2019.06.004.
- XXVII. Y. S. Mezaal, H. T. Eyyuboglu, and J. K. Ali, "Wide Bandpass and Narrow Bandstop Microstrip Filters based on Hilbert fractal geometry: design and simulation results," PLoS One, vol. 9, no. 12, p. e115412, 2014.
- XXVIII. Yang, Shuai, and Lajos Hanzo. "Fifty Years of MIMO Detection: The Road to Large-Scale MIMOs." *IEEE Communications Surveys & Tutorials*, vol. 17, no. 4, 2015, pp. 1941–1988. 10.1109/COMST.2015.2459053.
  - XXIX. You, Xiaohu, et al. "Towards 6G Wireless Communication Networks: Vision, Enabling Technologies, and New Paradigm Shifts." *Science China Information Sciences*, vol. 64, no. 1, 2021, pp. 1–74. 10.1007/s11432-020-2955-6.
  - XXX. Y. S. Mezaal, H. T. Eyyuboglu, and J. K. Ali, "New dual band dual-mode microstrip patch bandpass filter designs based on Sierpinski fractal geometry," in 2013 Third International Conference on Advanced Computing and Communication Technologies (ACCT), 2013. 10.1109/ACCT.2013.55
  - XXXI. Y. S. Mezaal and K. Al-Majdi and , "New miniature narrow band microstrip diplexer for recent wireless communications," Electronics, vol. 12, no. 3, p. 716, 2023. 10.3390/electronics12030716.
- XXXII. Zhang, C., and R. C. Qiu. "Massive MIMO Testbed—Implementation and Initial Results in System Model Validation." *arXiv*, 2014. arXiv:1501.00035. URL: https://arxiv.org/abs/1501.00035.
- XXXIII. Zhang, J. A., et al. "Multibeam for Joint Communication and Radar Sensing Using Steerable Analog Antenna Arrays." *IEEE Transactions on Vehicular Technology*, vol. 68, no. 1, 2019, pp. 671–685. 10.1109/TVT.2018.2888708.
- XXXIV. Zheng, Kan, et al. "Survey of Large-Scale MIMO Systems." *IEEE Communications Surveys & Tutorials*, vol. 17, no. 3, 2015, pp. 1738–1760. 10.1109/COMST.2015.2425294.